

AN ATLAS FOR INTERPRETING γ -RAY PULSAR LIGHT CURVES

KYLE P. WATTERS¹, ROGER W. ROMANI¹, PATRICK WELTEVREDE² & SIMON JOHNSTON²

(Received October 14, 2008)
Draft version October 24, 2018

ABSTRACT

We have simulated a population of young spin-powered pulsars and computed the beaming pattern and light curves for the three main geometrical models: polar cap emission, two-pole caustic (“slot gap”) emission and outer magnetosphere emission. The light curve shapes depend sensitively on the magnetic inclination α and viewing angle ζ . We present the results as maps of observables such as peak multiplicity and γ -ray peak separation in the (α, ζ) plane. These diagrams can be used to locate allowed regions for radio-loud and radio-quiet pulsars and to convert observed fluxes to true all-sky emission.

Subject headings: gamma-rays - pulsars - stars: neutron

1. INTRODUCTION

With the successful launch of the *Fermi Gamma-ray Space Telescope*, formerly *GLAST*, many pulsars are expected to be detected in the γ -ray band. This is an important opportunity since \sim GeV γ -ray emission dominates the observed electromagnetic output of young pulsars. Also, some pulsars are expected to be detected in the γ -ray band but undetectably faint in the radio. The natural interpretation is that the radio and γ -ray antenna patterns differ. Indeed, the observed pulsars have very different radio and γ -ray pulse profiles. Since the observed pulse profile is simply a cut through this antenna pattern for the Earth line-of-sight angle ζ_E , interpretation of the radio and γ -ray profile requires a beaming model. When the spin geometry is known, observed pulses can be used to select the best model. Conversely, for a given model, the pulse pattern can restrict the spin orientation. Finally, beaming corrections can be used to relate the observed line-of-sight flux to the full-sky emission. Thus, aided by beaming models, γ -ray pulsar data can give a new window into the energetics and evolution of neutron stars in the Galaxy.

There are three main geometrical models for the γ -ray pulse beaming, each tied to locations in the magnetosphere where force-free perfect MHD ($\vec{E} \cdot \vec{B} = 0$) conditions break down and the uncanceled rotation-induced EMF $\vec{E} \approx r\vec{\Omega} \times \vec{B}/c$ causes particle acceleration and radiation. These are the so-called magnetospheric gaps. The first γ -ray (and radio) pulsar models traced emission to acceleration zones on the field lines at very low altitudes above each magnetic pole (although Daugherty & Harding 1996 argued that such “polar cap” model emission could extend to $\sim 2R_*$). Another major class of models posits “Holloway” gaps above the null charge surface, extending toward the light cylinder (the “outer gap” model; see Cheng, Ho, & Ruderman 1986; Romani 1996). More recently, it has been argued that the true null charge location depends on currents in the gap (Hirovani 2006), allowing the start of the outer gap to migrate inward towards the stellar surface. Conversely, it has been argued that acceleration at the rims of the polar caps may extend to very high altitude (Muslimov & Harding 2004), effectively pushing the polar cap activity outward. Together these effects suggest that

emission can occur over a large fraction of the boundary of the open zone. One model that has been suggested for this geometry makes low-altitude emission visible from one hemisphere and higher-altitude emission (i.e., above the null charge surface) visible from the other. This is the “two-pole caustic” (TPC) model (Dyks & Rudak 2003), which is thus intermediate between the polar cap (PC) and outer gap (OG) pictures.

2. SIMULATION METHOD

We start by building a library of pulsar antenna patterns. We follow standard practice in basing our beaming on the retarded potential (Deutsch 1955) magnetic dipole fields. This has the appreciable advantage of analytic simplicity, allowing rapid computations. Numerical models of force-free magnetospheres do exist (Spitkovsky 2006), but such models do not have the resolution required for the sort of beaming computations pursued here and in any case do not, by definition, include acceleration gaps. Still, it should be remembered that magnetospheric charges and currents may well have an observable effect on the field structure and pulse shapes computed here.

We model the last closed field line surface (those field lines tangential to the speed of light cylinder at $r_\perp = r_{LC} = cP/2\pi$), tracing these field lines to the polar cap surface at the stellar radius r_* . The relevant magnetospheric features in the OG and TPC models are tied to the light cylinder and locations identified as fractions thereof; thus, the period of the pulsar is an unnecessary parameter in mapping the structure of the magnetosphere. Models are computed across all possible magnetic inclinations α . We follow the field line structure to $<10^{-4}r_{LC}$, allowing precision mapping of the PC emission region even for pulsar periods >1 s. A single magnetosphere model can serve a range of pulsar periods by truncating the grid at larger fractions of r_{LC} for shorter period pulsars, thereby maintaining the same physical distances. General relativistic effects make small changes for $r < 3r_*$ but are not included in the present sums.

In all models, the acceleration gap is inferred to arise near the open zone boundary tied to the last closed field lines. For the PC picture, we simply follow radiation emitted tangentially to these field lines at altitudes $\leq 1R_*$. In the original definition of the TPC model (Dyks & Rudak 2003) the emission was similarly placed on the last closed field lines but extended to an altitude $r < r_{LC}$ and a perpendicular distance $r_\perp < 0.75r_{LC}$, where r_{LC} is the *perpendicular* distance to

Electronic address: kwatters@stanford.edu

¹ Department of Physics, Stanford University, Stanford, CA 94305

² Australia Telescope National Facility, CSIRO, P.O. Box 76, Epping, NSW 1710, Australia

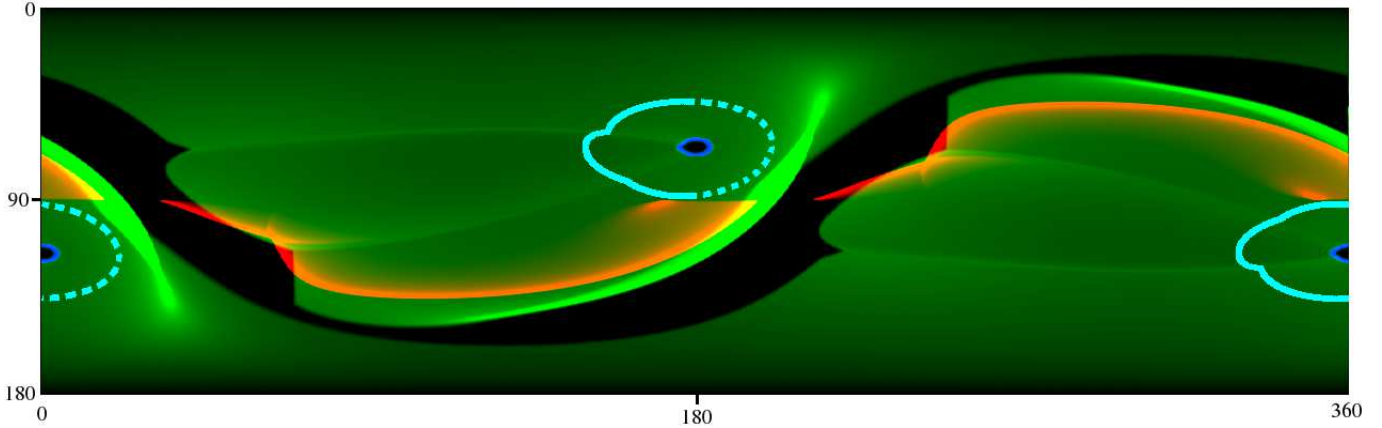


FIG. 1.— Sample antenna intensity patterns for $\alpha = 65^\circ$ with the horizontal axis of pulsar phase (ϕ) and vertical axis of viewing angle (ζ). The TPC model for $w = 0.05$ is shown in green, the OG model for $w = 0.1$ is shown in red and the PC emission site is shown in blue. The cyan lines show the locus of the possible high altitude ($r = 500$ km, here for $P = 0.2$ s) radio emission, with the radiating front half shown solid and the back half dashed (see §3.3).

the light cylinder from the rotation axis. In the outer gap (OG) model the emission is from a full set of open field lines associated with the closed zone surface, but pair production and radiation are expected to start above the null-charge surface [$\vec{\Omega} \cdot \vec{B}(R_{NC}) = 0$].

In any physical model, however, there should be an open zone vacuum region separating the surface of last closed field lines from the pair formation front, which defines the radiating surface of the gap. The OG model of Romani (1996) defined gap thickness w as the fraction of the angle from the last closed field line to the magnetic axis that remains a charge-starved vacuum with a large acceleration field. This characteristic gap width w is proportional to the γ -ray efficiency (see below). A physical TPC model should also have a finite gap thickness; the “slot gap” model of Muslimov & Harding (2003) provides a possible physical foundation for the TPC picture. These authors give an estimate for the dependence of gap thickness on spin period P and surface magnetic field B ; again the thickness increases for pulsars putting a larger fraction of the spindown power into pulsed γ -rays. Thus, for both models, we assume that the gap thickness can be related to a heuristic γ -ray luminosity

$$L_\gamma \approx \eta \dot{E}_{\text{SD}} \approx C \times \left(\frac{\dot{E}_{\text{SD}}}{10^{33} \text{ erg s}^{-1}} \right)^{1/2} \times 10^{33} \text{ erg s}^{-1} \quad (1)$$

with C , a slowly varying function of order unity which must come from a detailed physical model. This law, which assumes a γ -ray efficiency ($w = \eta \propto \dot{E}_{\text{SD}}^{-1/2}$), is natural in models that maintain a fixed voltage drop across the acceleration gap. Clearly, as $w \rightarrow 1$ this simple geometrical approximation should break down. The original TPC formulation has $w = 0$. In a full physical model, the radiating pair formation front would have a finite thickness and the radiation pattern of the particles would have a finite width; these effects are not treated here but would serve to smooth out the beams computed in the basic geometrical model. Sample antenna patterns (sky maps of the pulsar beam) are shown for the three models in Figure 1.

In each case, the antenna pattern is built up by Monte Carlo simulation. Radiation is emitted uniformly along the gap surface. The photons are aberrated, the time of flight to a distant observer is computed and the emission is assigned to a bin of pulsar phase and co-latitude (the sky map antenna pattern; see Romani & Yadigaroglu 1995; Dyks, Harding, & Rudak

2004). We normalize this antenna pattern by summing emission at all pulsar phases ϕ and along all lines-of-sight ζ and scaling by the heuristic γ -ray luminosity (Equation 1).

Although we focus here on the beaming characteristics rather than the population, to obtain a realistic sample of pulsar spin properties we simulate a Galactic population of young pulsars following the method of Weltevrede & Johnston (2008a). Pulsars are assigned a P and \dot{P} from the parent distribution of Weltevrede & Johnston (2008a). Since we are interested in energetic pulsars, we retain objects with $\dot{E} > 10^{34}$ (i.e., a max characteristic age $\tau = P/2\dot{P} \approx 10^6$ y), drawing until we have a sample of $\sim 175,000$ pulsars. This is $\sim 12\times$ the true Galactic density (given a birthrate of ~ 1.5 per century); the over-density serves to decrease statistical fluctuations. Magnetic inclinations α and Earth viewing angles ζ were drawn isotropically. Given the low upper limit on age, we ignore any possible magnetic alignment, which, if present, appears to occur on longer time scales. For each drawn pulsar the appropriate γ -ray light curve is computed for the drawn line-of-sight ζ using the appropriate antenna pattern from the library of sky maps.

While we do use a realistic pulsar population, we do not report here on predictions for the statistical distributions of γ -ray pulse shape, luminosity and Galactic location. These, and predictions for the relative numbers of radio-loud and radio-quiet pulsars expected in the LAT sky survey, are deferred to a subsequent paper. We also do not treat here the millisecond pulsar population, as with small light cylinder radii the difference between inner magnetosphere and outer magnetosphere emission zones is less stark.

2.1. Radio Emission

Radio beam models have a long history but are, if anything, even more heuristic than those for the GeV γ -rays. Here we consider two scenarios. One is simple low-altitude emission, which assumes a circular cone of radio emission along the last closed field lines with an angular width

$$2\rho = 10.8P^{-1/2} \text{ degrees} \quad (2)$$

centered on the magnetic axis (Rankin 1993; Gould 1994). Here, ρ is the half-opening angle of the radio cone; the scaling is well supported by observations, which also agree with the beam being roughly circular, as expected from dipole field line structure at moderate altitudes. To model this scenario

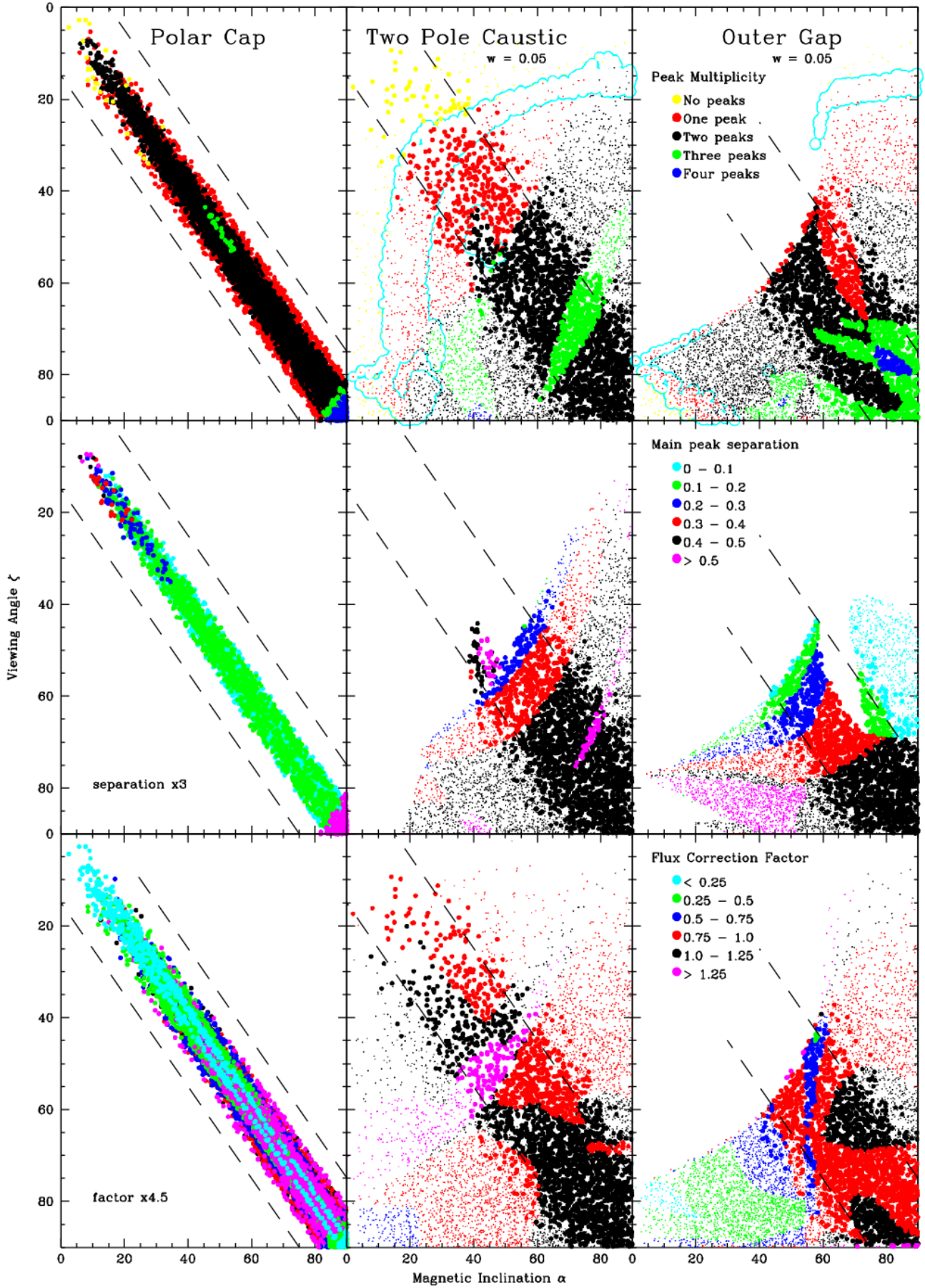


FIG. 2.— An atlas of pulse profile properties for three γ -ray pulsar models. Top row: pulse complexity (peak number); broad peaks lie in zone enclosed by the cyan lines. Middle row: pulse width Δ , the maximum separation of the major peaks. Bottom row: the “flux conversion factor” f_{Ω} for correction to all-sky flux. For the PC model, the small ranges of Δ and f_{Ω} require re-normalization of the color scale for those panels.

in our baseline computations we assume radio observability whenever the line of sight passes within ρ of the magnetic axis. The radio pulse peak is assumed to be at the same phase as this axis.

Recent evidence, however, suggests that young, Vela-like pulsars have a fixed emission altitude of $\sim 500 - 1000$ km or $\sim 30 - 70 R_*$ (Karastergiou & Johnston 2007). Since these are the dominant denizens of the γ -ray pulsar population, we also (see §3.3) consider the effect of such wide beams at higher altitude. This wide beam emission is assumed to be patchy, with some lines of sight crossing the radio zone but receiving negligible flux (Lyne & Manchester 1988). This is difficult to treat, except statistically, and is only discussed qualitatively in this work. As we shall see in §3.3, it is useful to consider the possibility that the leading portion of the radio zone has higher occupancy than the trailing half. We thus also compute radio pulse observability for emission only along the leading edge of a 500 km altitude radio emission zone (Figure 1). Aberration and light travel effects are computed for all radio pulses as well.

2.2. Pulse Profile Characterization

We wish to summarize the properties of the γ -ray pulses of the simulated population. We start by flagging the major peaks for each light curve, generated from cuts at a given ζ across antenna patterns such as those in Figure 1. Examples of light curves for these models can be seen in Figure 5 of Dyks, Harding, & Rudak (2004) for the particular case $\alpha = 60^\circ$. In the Appendix we show two summary figures of the light curves for a range of α and ζ (and w) for the OG and TPC models.

We have created a peak-finding routine that runs on the γ -ray light curves produced from the models. The light curves are searched for maxima that rise above the local minimum by least 20% of the global light curve maximum. Most non-thermal pulsar peaks are relatively narrow, so we flag “sharp” peaks by requiring that the full width at half maximum (FWHM) of the qualifying peak (i.e. measured at 10% of the full pulse amplitude below the peak maximum) have $\Delta\phi < 0.1$. The bright EGRET pulsars with high S/N light curves (Crab, Vela and Geminga) all show two peaks using this cut. However, wider maxima may also be of interest, so we additionally flag “broad peaks” with FWHM $0.1 < \Delta\phi < 0.3$. These tend to appear when either ζ or α is small. Note that some pulsars with both small ζ and α have appreciable γ -ray flux but show only shallow sinusoidal variations with no strong “peaks” as defined by the above algorithm.

Two additional key values regarding peak locations are also recorded. First, we record the separation from the first peak to the last peak. Additionally, we measure the lag of the first peak from the radio pulse. To help the reader understand the results of this peak flagging, in the Appendix figures we record the number of peaks, the broad peaks and the pulse width (in %) as determined by this routine for each of the plotted light curves.

Finally, we compute f_Ω , the ratio between the simulated total emission of the pulsar over all observer angles ζ and the total emission if the observed flux at ζ_E were emitted uniformly across the sky.

3. RESULTS

We have collected the geometrical pulse properties of the three models into an “atlas” (Figure 2) that compactly summarizes many complex pulse profiles. We plot simulated pul-

sars in the (α, ζ) plane, color coding the points to show the model properties. Small dots show objects detected in γ -rays but not in the radio. Radio detectable objects tend to lie at small $\beta = \zeta - \alpha$, the magnetic pole impact angle. The dashed lines show the low-altitude standard radio detection window for $P = 0.2$ s, the median for the observable γ -ray pulsar population. Of course, these are not strict boundaries; pulsars with large P have smaller radio pulse widths and may remain radio invisible at smaller β while especially fast pulsars may be radio detected well beyond the plotted lines. There are radio-detectable, γ -invisible objects as well. These are generally found at small α, ζ and are not plotted here.

The top row shows the pulse complexity, the number of major pulse peaks, with broad peaks appearing in the cyan curve. The second row shows, for each model, the phase interval Δ between the most widely separated major peaks. These plots may be used to predict the γ -ray properties for a given model and known orientation angles. Conversely, for an observed γ -ray pulse profile one may restrict the allowed viewing angles for a given model or even rule a model out completely. Of course, objects with well-constrained viewing geometry and observed profiles are particularly useful as they allow the most strict discrimination between pulse models. More generally, the distribution of observed pulse shapes is different between the models. Once one assumes an underlying pulsar distribution, such population analysis is also a very powerful discriminant (Watters et al. 2009).

The final row of the atlas depicts a flux correction factor f_Ω , useful in calculation of γ -ray efficiencies. The pulse profile observed along the line of sight at ζ for a pulsar with magnetic inclination α is $F_\gamma(\alpha, \zeta, \phi)$, which we can compute for a given pulsar model. This means that the observed phase-averaged flux F_{obs} for the Earth line-of-sight ζ_E is not necessarily representative of the flux averaged over the sky. This has also been emphasized by Harding, Grenier & Gonthier (2007). Here, we can use our model to compute the required correction f_Ω , so that the true luminosity is

$$L_\gamma = 4\pi f_\Omega F_{\text{obs}} D^2. \quad (3)$$

where D is the distance to the pulsar and

$$f_\Omega = f_\Omega(\alpha, \zeta_E) = \frac{\iint F_\gamma(\alpha, \zeta, \phi) \sin(\zeta) d\zeta d\phi}{2 \int F_\gamma(\alpha, \zeta_E, \phi) d\phi}. \quad (4)$$

It has become traditional to assume that the γ -ray beam covers an area of 1 sr uniformly, so that $f_\Omega = 1/(4\pi) \approx 0.08$; however, more modern pulsar beaming models have $f_\Omega \sim 1$ for many viewing angles.

The flux correction factor is crucial for estimating the γ -ray efficiency

$$\eta = L_\gamma / \dot{E}_{\text{SD}} \propto f_\Omega. \quad (5)$$

Thus, it appears that many recent papers have underestimated the true γ -ray efficiency (for modern pulsar models) by an order of magnitude.

From our heuristic luminosity law, we expect that the efficiency evolves as $\eta \propto \dot{E}_{\text{SD}}^{-1/2}$. In general, one would expect a larger fraction of the gap to remain charged-starved for more efficient pulsars, with $w \propto \eta$. In figures 3 and 4, we see how the pulse width and sky covering factor evolve with $w \equiv \eta$. In particular, for low- \dot{E}_{SD} , large- w , high-efficiency pulsars, we see that f_Ω decreases. Thus, the correction of observed phase average flux to true sky flux becomes a function of spindown power. As w saturates at a large value of order unity, which

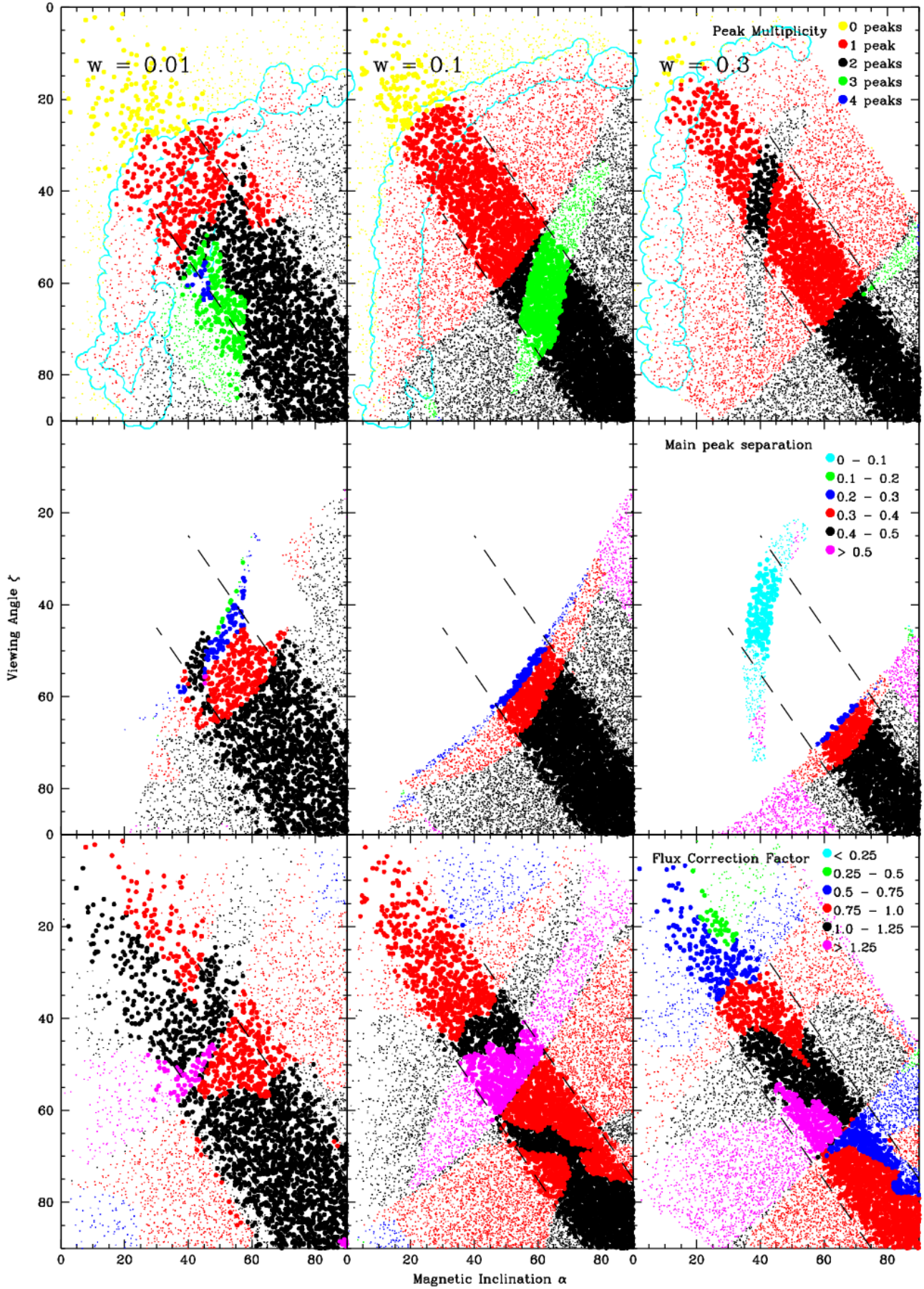


FIG. 3.— Beam shape evolution with efficiency for the TPC model. The three rows show peak complexity, peak separation and flux conversion factor, as in Figure 2. The gap width (and hence γ -ray efficiency) increases left to right.

for this calculation is near $\dot{E}_{SD} = 10^{33} \text{erg s}^{-1}$, no radiating surfaces bound the gaps and γ -ray production ceases. The exact value depends on magnetic inclination α .

For the convenience of other researchers, we have collected approximate fitting formulae for f_{Ω} , the flux correction factor. Because of the complexity of the beam patterns, it is always best to use the atlas figures to determine f_{Ω} for a pulsar with known parameters. However, statistical statements about luminosity and rough population sums can benefit from analytical approximations. For both the TPC and OG models there is a change in the beaming behavior at large α and ζ . In this region one sees emission from the hollow cone above the null charge surface that dominates the pulsation for the classical OG and often provides the late pulses in the TPC picture. We call this ‘‘case I’’ and thus define an approximate boundary for such objects as

$$\zeta > \zeta_I = (75 + 100w) - (60 + 1/w)(\alpha/90)^{2(1-w)}, \quad (6)$$

with ζ in degrees. Any pulsars with $\zeta < \zeta_I$ compose case II. For the OG scenario, $< 10\%$ of the modeled pulsars have any emission at smaller ζ , so case II is not a major contributor to the population. Such objects do, however, exist: principally pulsars with small w and large inclination α that are observed at small ζ . The emission comes from diverging high-altitude field lines producing faint γ -ray emission (often with no strong pulse) over much of the sky. In the TPC model, however, there is substantially more emission in case II, since the flux at these angles arises from low-altitude field lines viewed relatively near the polar cap. These light curves tend to show shallow sinusoidal pulses. They are also missing the caustic peaks (sharp pulses) dominating the case I objects. Thus, in both the TPC and OG models, Equation 6 defines a boundary past which the pulse emission is fainter and f_{Ω} is larger. Figures 2-5 and the light curves in the Appendix (Figures 9 and 10) make these patterns clear.

For the TPC model, we find in the case I zone

$$f_{\Omega} \approx 0.8 + 1.2(0.3 - w)\cos(2\beta), \quad (7)$$

where $\beta = \zeta - \alpha$. This applies for pulsars with $w > 0.05$ and gives estimates accurate to 10% for 76% of the pulsars and to 20% for 90% of the pulsars. In the case II zone the flux correction factors are generally larger, with

$$f_{\Omega} \approx 0.3 + 1.5(1 - w)[1 + (\zeta - \zeta_I)/90]. \quad (8)$$

This region also has more complex behavior, so it is better to use the atlas figures if possible. The overall accuracy for the TPC model estimates (case I and case II zones together) is better than 10% for 62% of the modeled objects and within 20% for 82% of all modeled pulsars.

For the OG we consider the case I zone only, finding

$$f_{\Omega} \approx 0.17 - 0.69w + (1.15 - 1.05w)(\alpha/90)^{1.9} \quad (9)$$

for $\zeta > 60^\circ$. A ζ -dependent term appears for pulsars viewed closer to the spin axis, so that

$$f_{\Omega} \approx 0.17 - 0.69w + (1.15 - 1.05w)(\alpha/90)^{1.9} - 1.35(2/3 - \zeta/90) \quad (10)$$

when $\zeta < 60^\circ$. These give approximations accurate to better than 10% for 70% of the simulated case I pulsars with $w > 0.05$ and are better than 20% for 92% of such pulsars. The atlas figures give a guide to regions where exceptions occur.

3.1. Determining Individual Pulsar Geometries

Many young energetic pulsars produce bright, resolvable X-ray pulsar wind nebulae (PWNe), the beam dump of relativistic particles and fields flowing out of the magnetosphere. Often, high-resolution X-ray images of these PWNe can be interpreted in terms of cylindrically symmetric structures, with a mildly relativistic ($v \approx 0.3 - 0.7c$) bulk outflow Doppler-boosting the intensity along the radial flow. The inference is that the symmetry axis traces the pulsar spin, and fits to such models (Ng & Romani 2008) can provide relatively model-free estimates of ζ_E . Thus, for such pulsars, the family of allowed models is given by horizontal slices across the atlas panels.

Since we are concerned with detected γ -ray pulsars, one will inevitably have an estimate of the pulse width Δ . This is, then, the most robust observable, and provides a key to determining the rest of the model parameters. Thus, the prescription for solving a pulsar for a given model is to *i*) use \dot{E}_{SD} (Equation 1) to estimate w ; *ii*) go to the atlas pulse width plot for the closest w and locate regions showing a suitable Δ ; *iii*) use an external value for ζ_E , when available, to locate the relevant point in the Δ band and confirm that that the pulsar is radio loud or quiet, as appropriate; *iv*) use the ζ and α values for this point to read off other pulsar properties (Figures 2-4). Since the Δ plot is the ‘‘key’’ to the atlas, and since there are large regions at high α and ζ with $\Delta \sim 0.4 - 0.5$, especially for the TPC model, we provide in Figure 5 an expansion of the lower right quadrant of the evolving Δ panels with finer color bands. This should be used to determine ζ and α when possible, which can be transferred to Figures 3 and 4.

There is also a well-developed phenomenology connecting the sweep of linear polarization within the radio pulses to cuts across a simple magnetic pole. In the classic rotating-vector model (RVM, Radhakrishnan & Cooke 1969), the emission is assumed to have a polarization vector locked to the dipole magnetic field (projected on the plane of the sky) in the emitting region. The shape of the polarization sweep depends most sensitively on the value $\sin(\alpha)/\sin(\beta)$. As β generally takes on small values (or else the object would not be detected in the radio in the first place), this method tends to give poor constraints on α and tighter constraints on β . Thus, in principle, X-ray and radio data together can provide both ζ and α and therefore a prediction of the γ -ray pulse shape.

In practice, the picture is often not this simple. One possible complication arises if the altitude of the radio emission is large, where sweep-back and time-delay can alter the naive rotating-vector model predictions (Everett & Weisberg 2001). Finally, we should reiterate that our models are purely geometrical (albeit motivated by physics) and locked to the vacuum dipole field. Field-line perturbations, currents and variation in emissivity along the gap can all perturb the profiles. Nevertheless, this atlas does capture the key differences between the models and provides a basis for broad-brush interpretation of newly discovered pulsars.

3.2. The Polar Cap Model

The polar cap picture naturally predicts that only pulsars seen at small β will be seen in the γ -rays. With the radio emission originating above the surface γ -rays (which are at $r \lesssim 2r_*$), one would always expect radio emission bracketing the GeV pulse. ‘‘Radio-quiet’’ objects, such as Geminga, are not possible in this picture unless the radio cone is very patchy and emission is completely absent along ζ_E . ‘‘Inter-

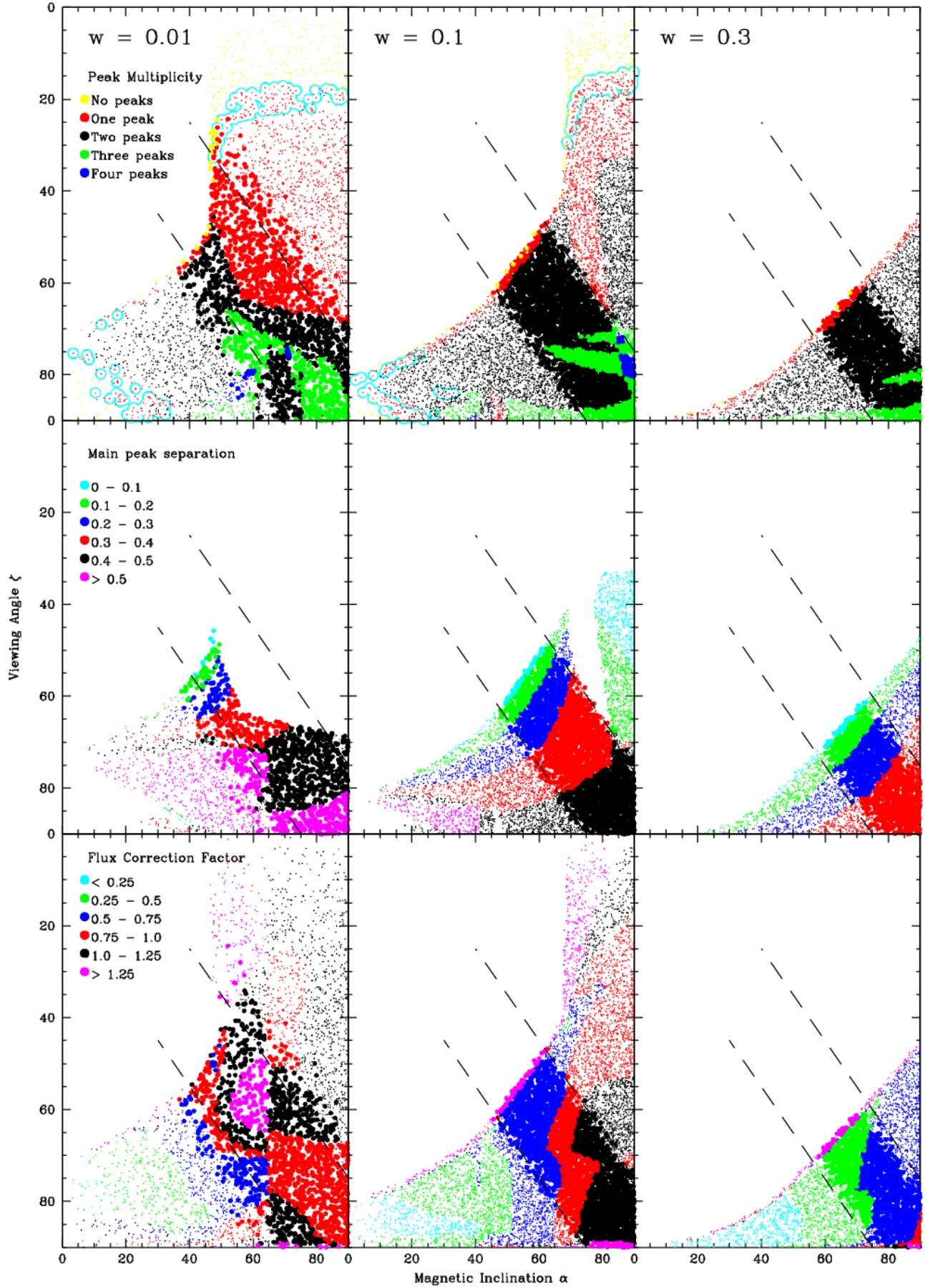


FIG. 4.— Outer Gap model beam shape evolution as a function of gap width, as in Figure 3.

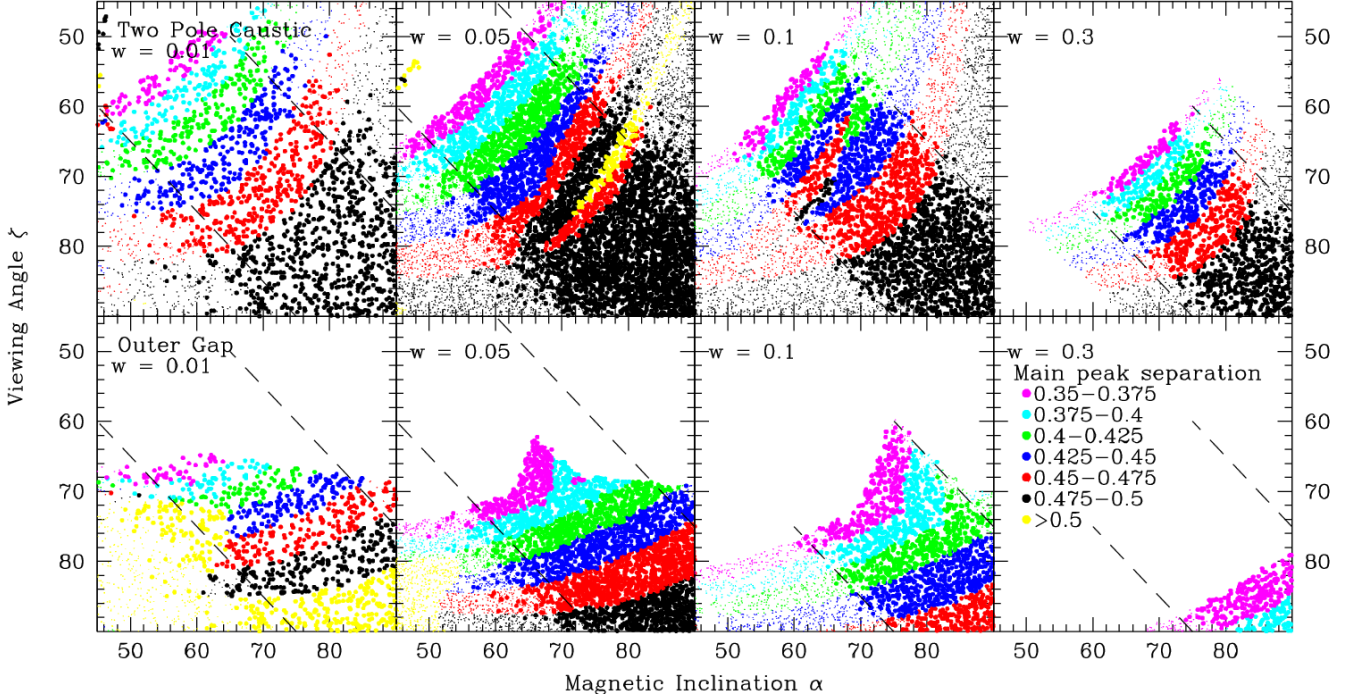


FIG. 5.— The pulse width for TPC and OG models at several w . This figure should be used when possible to locate accurately the α and ζ for a given pulsar, for reference back to Figures 3 and 4.

pulsars,” with emission visible from both radio poles, are expected at the lower right ($\alpha \sim \zeta \sim 90^\circ$), where the left panel of Figure 2 shows triple- and quadruple-peaked light curves for this model. Note that there is also a small collection of triply-peaked light curves at $\alpha \sim \zeta \sim 45^\circ$ stemming from the notch structure observed in the outline of the polar cap for inclination angles $\alpha \sim 45^\circ$ (Dyks, Harding, & Rudak 2004).

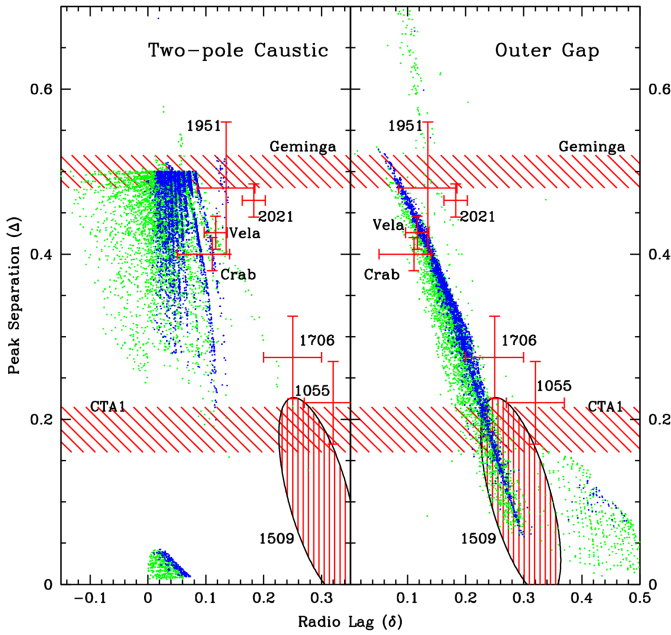


FIG. 6.— Pulsar γ -ray peak separation vs. radio lag. Green points are radio-quiet γ -ray pulsars, blue points are radio-loud γ -ray pulsars.

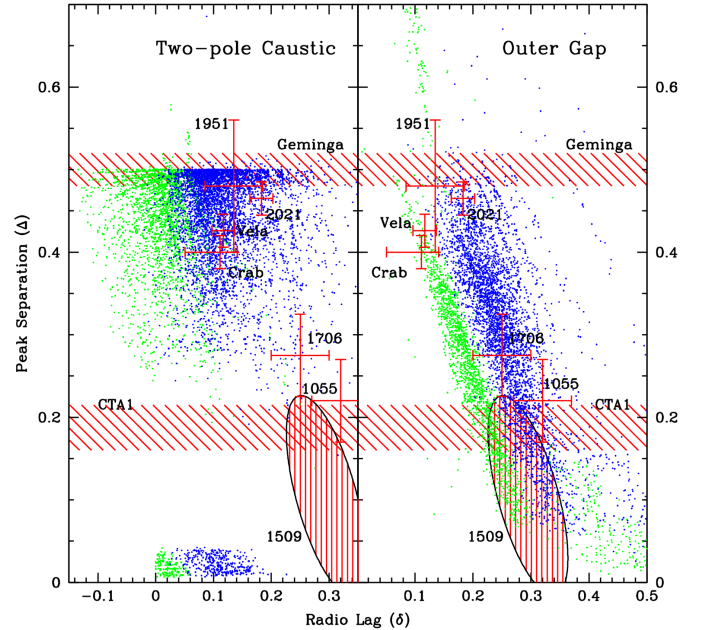


FIG. 7.— As Figure 6, but assuming high-altitude radio emission from the leading half of the radio zone.

The wide double pulses, with $\Delta = 0.35 - 0.45$, seen for the bright EGRET pulsars pose another challenge to the PC model. While a double-pulse light curve is the dominant mode in the PC zone, a wide separation can only be obtained for very small α and a small range of ζ . Unless pulsars are born highly aligned, this is statistically very improbable. Additionally, model-independent measurements of ζ made through the analysis of PWN tori mentioned above have consistently found values $\zeta > 40^\circ$, well beyond the

range for which the polar cap model can produce large peak separations.

These geometrical arguments, as well as considerations of flux and spectrum, imply that the bulk of the observed γ -ray pulsar emission seen by EGRET could not have come from a low-altitude cap. However, if a surface gap does have active pair production, some γ -rays are nevertheless expected from this region; very sensitive *Fermi* LAT observations may be able to uncover such a component.

3.3. Observed Pulsars

The atlas lets one read off the expected γ -ray pulse properties for known α and ζ or estimate from Δ values for undetermined α and ζ . It is also interesting to compare the observed properties of specific pulsars with the models' predictions. Table 1 lists the observed properties of the well known EGRET pulsars and two new detections, J2021+3651 from *AGILE* (Halpern et al. 2008) and CTA 1 from *Fermi* (Abdo et al. 2008). Column 4 lists the externally derived values for the line-of-sight angle ζ , when available.

Note that for PSR B1055–52 the radio-derived ζ accords well with the value predicted by the γ -ray pulse width Δ in the outer gap picture. The TPC picture does have a solution matching the observed Δ (albeit only for w much lower than inferred from \dot{E}_{SD}), but ζ does not agree with the radio value, and additionally α is too small to produce the observed radio interpulse. For the two radio-quiet pulsars Geminga and PSR J0007+7303 in CTA 1 we do not have ζ estimates. For CTA 1, both OG and TPC models can match the observed Δ . For Geminga, with $\Delta = 0.5$, the TPC model has solutions along both the ζ and α axes. For the OG model, Geminga-type Δ are only natural at small α and large ζ , where one will almost certainly miss the radio beam.

In addition to the γ -ray pulse width Δ , for radio-detected objects, the lag δ of the first γ -ray pulse from the radio peak is a second convenient observable. In Figure 6 we have plotted in blue a sample of simulated γ -ray pulsars, in the $\Delta - \delta$ plane, assuming that the radio peak is centered along the magnetic axis. If the viewing angle ζ is too far from the pole (i.e., β large) then no radio pulse will be detected. In these cases we have plotted the pulsars in green, with δ the phase lag from the closest approach to the radio pole. For the TPC model, many of these pulsars have a first γ -ray peak leading the radio pole. Some known γ -ray pulsars with well defined pulse profiles have been placed on the figure. For the two “radio-quiet” pulsars Geminga and PSR J0007+7302, no δ is available, so the allowed regions are shown as horizontal bands. PSR B1509–58 was seen at MeV energies by *CGRO*, but was not convincingly seen by EGRET; its broad peak has a small but poorly defined Δ , so it appears as a diagonal band.

It is clear from Figure 6 that many of the observed radio/ γ -ray pulsars have a larger radio lag than expected in either the TPC or OG model if the radio pulse is centered on the magnetic axis. This suggests that some ingredient is missing from our basic geometrical model. One possibility is that magnetospheric currents sweep the γ -ray emitting field lines back to later phase. Alternatively, an extra lag may be connected with the posited high altitude radio emission of the young pulsars (Weltevrede & Johnston 2008b). If we invoke patchy emission and make the additional (new) assumption that the patches are most active on the leading half of the radio zone, then aberration and field-line spreading on this leading half of the cone can drive the high-altitude radio peak to much earlier

phases. The range of allowed lags is shown in Figure 7 for a fixed altitude of 500 km. Note that the phase lead δ then depends on the pulsar spin period, since this fixed altitude is a variable fraction of r_{LC} . These are the model tracks in Figure 7. Large β will result in a smaller increase in δ as the radio cone is cut with a small chord, further from the magnetic axis. Again for the green (radio-quiet pulsar) dots, we plot the δ from the closest approach to the radio pole. As expected, the wider radio pulse allows fewer green (radio non-detected) objects.

Finally, we should compare the model pulsar efficiencies η with the observed γ -ray fluxes, using our computed f_{Ω} . Of course, this is a purely geometrical comparison, ignoring real differences in γ -ray spectrum and the radiation processes tapping the primary electron energy. Nevertheless, the differences in f_{Ω} are substantial (and often completely ignored in discussions of η). For gaps with near-constant brightness and pulsars with well determined distances, the f_{Ω} variations can be the biggest unknown, making our treatment useful.

Table 1 contains the estimated f_{Ω} ranges inferred for the TPC and OG models. In Figure 8, we plot the inferred efficiencies of the detected γ -ray pulsars, after correction with f_{Ω} to simulated all-sky emission for the two models. The distance uncertainties generally dominate the range in the derived L_{γ} . The solid line shows complete conversion of spin-down power to γ -rays and the dashed line shows the heuristic efficiency law assumed above.

In Figure 8, two objects near $\log(\dot{E}) = 36.5$ deserve comment. The first is PSR J2021+3651 in the “Dragonfly” nebula. This has a very large dispersion measure, and the corresponding 12.4 kpc distance would imply $\geq 100\%$ efficient γ -ray production for both TPC and OG pictures. However, Van Etten, Romani, & Ng (2008) argue that a variety of pulsar and PWN measurements are more consistent with a distance of ≤ 3 kpc. In fact, the thermal surface emission has a best fit distance of $d = 2.1$ kpc; $d \sim 1.6$ kpc would bring this pulsar into agreement with the heuristic efficiency law. The origin of the large DM for this pulsar is thus very puzzling. The next outlier is PSR B1706–44, at similar \dot{E} , where we have adopted the DM distance of 2.3 kpc (Cordes & Lazio 2002). Again, smaller distances are implied by fits to the neutron star thermal emission and the PWN energetics (Romani et al. 2005), with preferred values at $d \leq 1.8$ kpc. However, to match the efficiency law would require distances close to 1 kpc; this is substantially below the statistical lower bound on the distance estimated from H I absorption (Koribalski et al. 1995). Thus, the Earth line-of-sight flux of these two Vela-type pulsars seems larger than predicted from their spindown luminosity and the beaming model. Improved flux measurements from the LAT and improved distance estimates (e.g., a radio interferometric parallax for PSR B1706–44) would be particularly valuable in tightening up this argument.

The most interesting region of Figure 8 is the low- \dot{E} range, where the modeled efficiencies approach unity. For these large w pulsars, f_{Ω} begins to drop significantly below unity, especially in the OG model, decreasing the effective L_{γ} . This effect dominates as pulsars approach the γ -ray death zone, near the end of their lives as high-energy emitters. The small f_{Ω} values prevent the apparent catastrophe of $L_{\gamma} > \dot{E}$ for old pulsars. Conversely, while a small fraction of such pulsars, with their γ -beams closely confined to the spin equator, are visible along the Earth line of sight, those that *are* seen have relatively high fluxes and are detectable to relatively large dis-

TABLE 1
GEOMETRY AND BEAMING OF BRIGHT EGRET PULSARS

Name	$\log(\dot{E}_{SD})$	w	d (kpc) ^a	ζ^b	Δ^c	δ^c	α_{TPC}^d	ζ_{TPC}^d	$f_{\Omega}(TPC)^d$	α_{OG}^d	ζ_{OG}^d	$f_{\Omega}(OG)^d$
Crab	38.7	0.001	2.0 ± 0.2	63	0.40	0.111	55-60	63	1.1	70	63	1.0
Vela	36.8	0.01	$0.287_{+0.019}^{-0.017}$	64	0.426	0.117	62-68	64	1.1-1.15	75	64	1.0
B1951+32	36.6	0.02	2.0 ± 0.6	...	0.48	0.135	55-90	55-90	1.0-1.25	60-90	70-85	0.75-1.1
B1706-44	36.5	0.02	2.3 ± 0.7	53	0.2	0.25	45-50	53	1.05	47-49	53	0.7-1.0
J2021+3651	36.5	0.02	3.0 ± 1.0	86	0.465	0.165	70	86	1.1	70	86	1.05
CTA 1	35.7	0.05	1.4 ± 0.3	...	0.20	—	55-70	23-45	0.8-1.3	20-50	60-75	0.3-0.9
Geminga	34.5	0.18	$0.25_{+0.120}^{-0.062}$...	0.50	—	30-80,90	90,55-80	0.7-0.9,0.6-0.8	10-25	85	0.1-0.15
B1055-52	34.5	0.18	0.72 ± 0.15	67	0.22	0.32	60 ^e	50	0.85	78	67	0.55

^a Distance references (in order): traditional for Crab; Dodson et al. (2003); Strom & Stappers (2000); Cordes & Lazio (2002); Van Etten, Romani, & Ng (2008); Abdo et al. (2008); Faherty, Walter, & Anderson (2007); Cordes & Lazio (2002).

^b From torus fits to X-ray images (Ng & Romani 2008) when available; B1055-52 from radio RVM fit (Lyne & Manchester 1988).

^c Derived from light curves in Fierro (1995) except J2021+3651 (Halpern et al. 2008) and CTA 1 (Abdo et al. 2008).

^d Estimated from Figures 2 and 4.

^e Requires $w \lesssim 0.1$

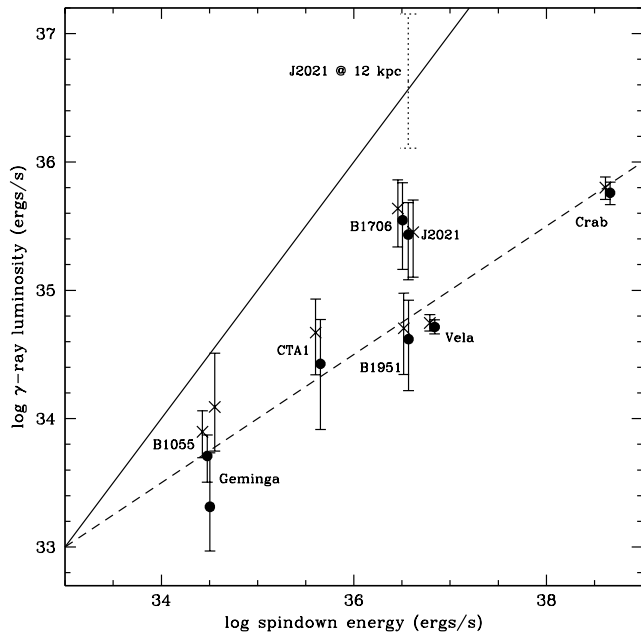


FIG. 8.— Derived γ -ray luminosity, corrected (TPC – crosses, OG – circles) from the observed phase-averaged flux to all-sky, vs. the spindown luminosity. Error bars include both the d and f_{Ω} uncertainties (Table 1). The dotted error bar at large L_{γ} represents the γ -ray luminosity of J2021+3651 assuming the DM distance of 12.4 kpc.

tances. Geminga is an excellent example.

4. DISCUSSION & CONCLUSIONS

Our study allows a quick visual summary of model predictions, which may be compared with pulsar discoveries anticipated from the LAT. We have already seen that the classic polar cap (PC) picture is difficult to reconcile with the data. Both the TPC and OG pictures, however, seem viable. Certain observations would clearly discriminate. For example, detection of γ -ray pulsars with $\alpha + \zeta < 90^\circ$, but with nearly constant intensity through the period, would give a clear preference for the TPC model. In contrast, the prevalence of light curves with simple double pulses separated by $0.05 < \Delta < 0.3$ is a hallmark of high-altitude OG emission. The distributions

in peak widths and in the relative number of radio-loud and radio-quiet pulsars are also a strong discriminant; we will address these in a following paper concentrating on the population statistics of detectable objects (Watters et al. 2009).

Also, the predicted pulse profile complexities for the two models differ. OG models are complex for $\alpha \sim \zeta \sim 90^\circ$; TPC models have complex profiles at intermediate α . In general, the radio-faint pulsars are double-peaked in both models, but the TPC picture has relatively more single- and zero-peaked solutions.

One area of agreement between the TPC and OG models is the preponderance of large f_{Ω} ; this is a principal result of our study: inferred efficiencies should be increased by roughly an order of magnitude from those commonly assumed. In practice this means that some young pulsars must have high ($> 10\%$) γ -ray efficiencies. This argues that a study of the γ -ray emission is an even better probe of magnetosphere structure and energetics than previously thought. Our f_{Ω} corrections tighten the well-known trend for efficiency to scale as $\eta \propto \dot{E}^{-1/2}$, although a few outliers remain. If, as more pulsars are discovered by the LAT, we find that this trend remains strong, we may even be able to use observed fluxes, after f_{Ω} correction, for “standard candle” estimates of pulsar distances. Such arguments suggest relatively low distances for PSRs J2021+3651 and B1706-44.

Importantly, for models with $w(\dot{E})$ increasing with age, f_{Ω} tapers off at small \dot{E} . Thus the sky coverage decreases smoothly into a “death zone” where the gap shuts off. Near shut-off, the small solid angle on the sky ensures that old pulsars appear relatively bright and are visible to large d . This will be an important signature in the population sums (Watters et al. 2009). Examination of the distribution of pulse properties over the simulated pulsar sample is thus the key to testing the models and to producing the corrected luminosities that will make LAT data powerful in probing pulsar populations and spindown.

K.P.W. was supported by NASA under contract NAS5-00147. We thank the referee, A. Harding, for several helpful suggestions that improve the utility of this paper.

REFERENCES

- Abdo, A.A. et al. 2008, Science, in press.
 Cheng, K.S., Ho, C., & Ruderman M.A. 1986, ApJ, 300, 522.
 Cordes, J.M. & Lazio, T.J.W. 2002, arXiv, astro-ph, 0207156.
 Daugherty, J.K. & Harding, A.K. 1996, ApJ, 458, 278.

- Deutsch, A.J. 1955, *Ann. d'Ap.*, 18, 1.
 Dodson, R., et al. 2003, *ApJ*, 596, 1137.
 Dyks, J. & Rudak, B. 2003, *ApJ*, 598, 1201.
 Dyks, J., Harding, A.K., & Rudak, B. 2004, *ApJ*, 606, 1125.
 Everett, J.E. & Weisberg, J.M. 2001, *ApJ*, 553, 341.
 Faherty, J., Walter, F.M., & Anderson, J. 2007, *Ap&SS*, 308, 225.
 Fierro, J.M. 1995, PhD Thesis, Stanford University.
 Gould, D.M. 1994, PhD Thesis, Univ. Manchester.
 Halpern, J.P. et al. 2008, *ApJ* L., 688, 33.
 Harding, A.K., Grenier, I.A. & Gonthier, P.L. 2007, *Ap&SS*, 309, 221.
 Hirotani, K. 2006, *ApJ*, 652, 1475.
 Jiang, Z.J. & Zhang, L. 2006, *ApJ*, 643, 1130.
 Karastergiou, A. & Johnston, S. 2007, *MNRAS*, 380, 1678.
 Koribalski, B., et al. 1995, *ApJ* 441, 756.
 Lyne, A.G. & Manchester, R.N. 1988, *MNRAS*, 234, 477.
 Manchester, R.N. 2005, *ApSS*, 297, 101.
 McLaughlin, M.A. & Cordes, J.M. 2000, *ApJ*, 538, 818.
 Muslimov, A.G. & Harding, A.K. 2003, *ApJ*, 588, 430.
 Muslimov, A.G. & Harding, A.K. 2004, *ApJ*, 606, 1143.
 Ng, C.-Y., & Romani, R.W. 2008, *ApJ*, 673, 411.
 O'Brien, J.T. et al. 2008, *MNRAS*, 388L, 1.
 Radhakrishnan, V. & Cooke, D.J. 1969, *ApL*, 3, 225.
 Rankin, J. 1993, *ApJ*, 405, 285.
 Romani, R.W. & Yadigaroglu, I.-A. 1995, *ApJ*, 438, 314.
 Romani, R.W. 1996, *ApJ*, 470, 469.
 Romani, R.W., Ng, C.-Y., Dodson, R., & Brisken, W. 2005, *ApJ*, 631, 480.
 Spitkovsky, A. 2006, *ApJ* Letters, 648, 51.
 Story, S.A., Gonthier, P.L., & Harding, A.K. 2008, *ApJ*, 671, 713.
 Strom, R.G. & Stappers, B.W. 2000, *ASPC*, 202, 509.
 Van Etten, A., Romani, R.W., & Ng, C.-Y. 2008, *ApJ*, 680, 1417.
 Watters, K., et al 2009, *ApJ*, in prep.
 Weltevrede, P. & Johnston, S. 2008, *MNRAS*, 387, 1755.
 Weltevrede, P. & Johnston, S. 2008, *MNRAS*, in press.
 Yadigaroglu, I.-A. & Romani, R. 1995, *ApJ*, 449, 211.
 Zhang, L., Cheng, K.S., Jiang, Z.J., & Leung, P. 2004, *ApJ*, 604, 317.

APPENDIX

Here we show a selection of light curves for the two-pole caustic (TPC) and outer gap (OG) models. For both, we arrange the sample light curves on an α , ζ grid so that the results may be compared with the “atlas” figures (Figures 2-4). Light curves are shown for four w values (0.01, 0.1, 0.2, 0.3). The number of peaks (total and broad only) and the maximum peak separation Δ (expressed here in %) as flagged by the automatic peak finder are given near the individual light curves.

These light curves allow the reader to visualize the topological parameters summarized in the color “atlas” figures. For example, in the TPC plot one can see the broad, sinusoidal profiles that arise at low α and ζ and thus earn the “zero major peak” classification. One also sees how the TPC model has complex pulses near $\alpha \sim 40^\circ$, $\zeta \sim 60^\circ$ and that these sometimes give small separations between the strongest peaks. For the OG plots, one sees that for $\alpha > 60^\circ$ and small ζ the normal first peak is often lost; this is a result of the rapid spreading of the high-altitude field lines contributing to this peak, which prevents formation of the sharp leading caustic. Also, one sees that the pulse shapes are often complex near $\zeta = 90^\circ$ and that the pulse shapes simplify toward basic double pulses as w becomes large.

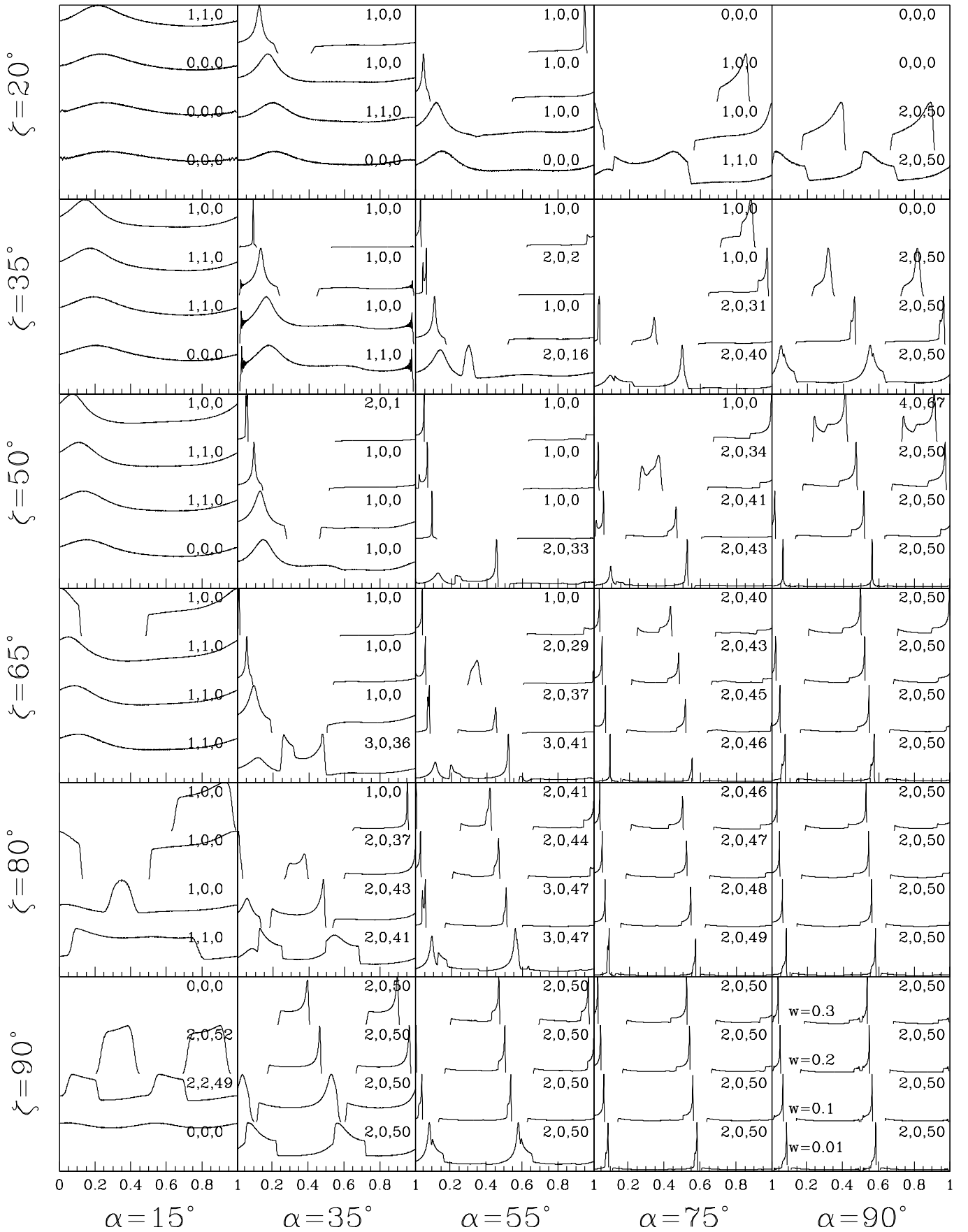


FIG. 9.— Collection of sample light curves for the TPC model. Four select w (values in bottom right panel) are shown for each panel; the radio pole has closest approach at phase=0. The values for the number of all peaks, the number of broad peaks and the maximum peak separation (in %) are indicated by each curve. Intensities are normalized to pulse maximum.

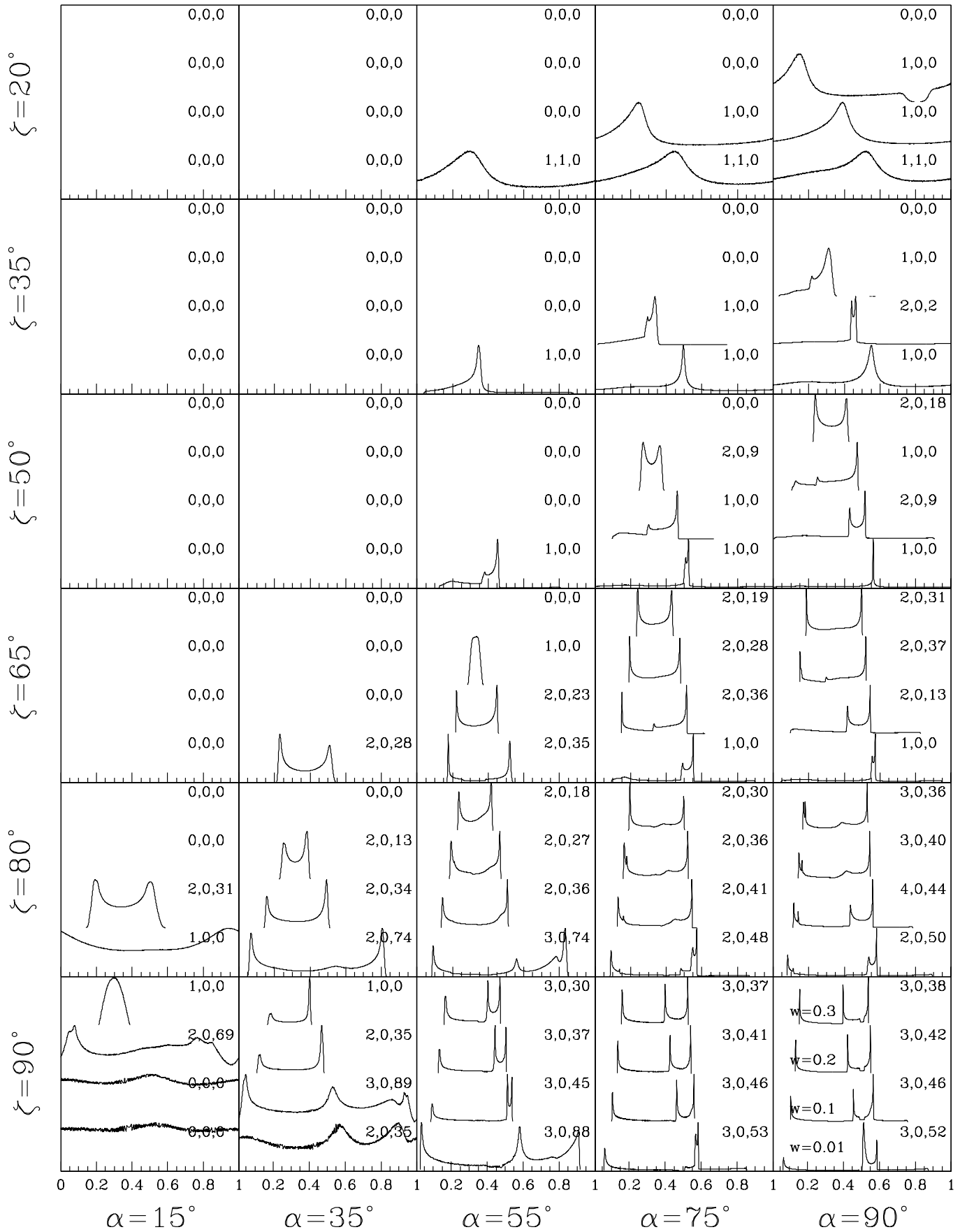


FIG. 10.— OG model light curves, as for Figure 9. Four select w (values in bottom right panel) are shown for each panel; the radio pole has closest approach at phase=0. Intensities are normalized to pulse maximum. For small α or ζ , especially at large w , no pulses form.